(Received 27 October 2025, Accepted 30 December 2025, Scheduled 21 January 2026)

GPR-SAR Imaging of Underground Pipelines Using Adaptive Threshold-Enhanced CBP Algorithm

Qiang Guo[1,2], Pengju Yang[1,2,*], Rui Wu[1,3], and Yuqiang Zhang[1]

[1] *School of Physics and Electronic Information, Yan'an University, Yan'an 716000, China*
[2] *Shaanxi Key Laboratory of Intelligent Processing for Big Energy Data, Yan'an University, Yan'an 716000, China*
[3] *Institute for Radio Frequency Technology and Software, Beijing Institute of Technology, Beijing 100081, China*

ABSTRACT: An adaptive threshold enhanced-Cross-correlation Back Projection (CBP) imaging algorithm is presented for artifacts suppression and accuracy improvement of Synthetic Aperture Radar (SAR) imaging in Ground Penetrating Radar (GPR) applications. B-Scan profiles of underground pipelines were obtained by using the open-source gprMax simulator, and they were then preprocessed using the background subtraction method to remove direct waves. An adaptive threshold scheme using Hilbert transform is adopted to obtain the envelopes of B-Scan profiles after removing direct waves. GPR-SAR imaging of underground pipelines is simulated and discussed in detail for different pipe parameters and soil environments. The simulated results demonstrate that the adaptive threshold enhanced-CBP algorithm achieves focused pipeline images with sub-wavelength localization accuracy, enabling geometric contour reconstruction for non-metallic pipelines with strong robustness in Peplinski's soil and multiple target scenarios.

1. INTRODUCTION

Underground pipelines constitute critical urban infrastructure for energy transmission, water supply, and drainage systems. However, rapid urbanization has resulted in disorderly pipeline distribution, aging damage, and management deficiencies, causing incidents such as water leaks, fires, and explosions. Therefore, the high-precision detection of underground pipelines has become an urgent necessity to ensure urban operational safety. Ground Penetrating Radar (GPR) is a geophysical exploration method that can conduct nondestructive testing (NDT) of underground targets or scenarios, leading to its widespread application in both military and civilian fields. With the development of GPR-SAR imaging at high resolution, the imaging algorithms have primarily focused on the Back Projection (BP) Algorithm [1], Diffraction Tomography (DT) Algorithm [2], Range Migration (RM) Algorithm [3], and Reverse Time Migration (RTM) Algorithm [4]. Among these algorithms, the DT algorithm achieves high imaging accuracy and enables the inversion of pipeline dielectric permittivity and electrical conductivity. However, its inversion process requires precise observation scenarios and strict approximation conditions, which substantially limit its practical applicability. Studies have shown that RM and RTM exhibit instability under heterogeneous media conditions between the GPR antenna and target, resulting in longitudinal positioning errors and artifacts [5, 6]. The BP algorithm is based on the delay-and-sum (DAS) beamforming algorithm. It fully considers the effects of the layered media between the antenna and target in imaging geometries, providing accurate electromagnetic wave refraction compensation at media interfaces. Therefore, this algorithm has been widely adopted for time-domain GPR-SAR imaging. However, images reconstructed by this algorithm contain negative values in GPR-SAR imaging, particularly at the edge of the target, which have no physical meaning and are essentially undesired artifacts [7]. In recent years, artifact suppression has attracted extensive attention from researchers. Foo and Kashyap proposed Cross-correlation Back Projection (CBP) algorithm, in which a reference signal far from the antenna center is required, increasing hardware costs and computational complexity [8]. Lim et al. introduced a delay-multiply-and-sum (DMAS) algorithm in medical imaging, enabling target reconstruction without additional reference channels [9]. Based on the DMAS algorithm, Zhou et al. proposed a novel CBP algorithm for effectively suppressing artifacts [10].

In this study, an adaptive threshold-enhanced CBP algorithm is presented for GPR-SAR imaging to locate and reconstruct underground pipelines. The B-Scan signatures of underground pipelines were simulated by using open source gprMax. To obtain more distinct hyperbolic features, the B-Scan profiles of underground pipelines are preprocessed by using the background subtraction method, and the envelopes of B-Scan profiles are then further extracted using the adaptive threshold scheme. Based on the extracted envelopes, the CBP was used for the location and reconstruction of underground pipelines.

This paper is organized as follows. Section 2 introduces the principle of GPR, the electromagnetic modeling (EM) of underground pipelines, adaptive threshold scheme, and the principle of CBP algorithm for GPR-SAR imaging. In Section 3, the results and analyses are presented, including the performance indexes of the CBP for focusing and restructuring different types of underground pipelines, which are also used to focus and restructure multiple pipelines. Section 4 concludes this study.

* Corresponding author: Pengju Yang (pjyang@yeah.net).

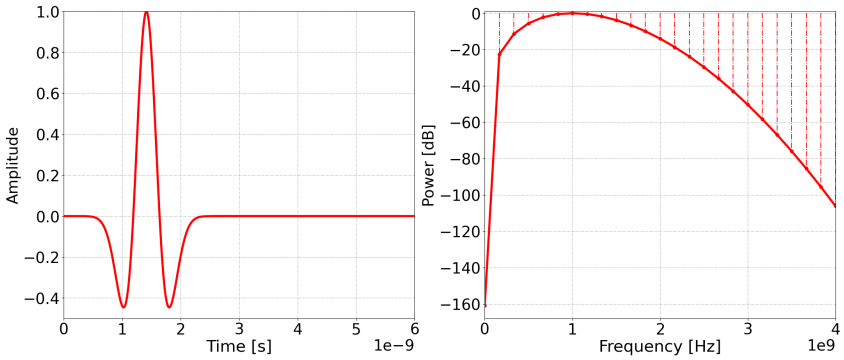

FIGURE 1. The time-domain and power spectrum for Ricker waveform.

2. METHOD

In this section, the complete data processing workflow for GPR-SAR imaging of underground pipelines is outlined. First, electromagnetic modeling of the buried pipelines was performed using gprMax to acquire raw B-Scan data containing the targets. Next, the background subtraction method was employed to remove direct wave interference, thereby enhancing the pipeline reflection signals. Subsequently, an adaptive thresholding method based on the Hilbert transform was utilized to extract B-Scan envelope data, further highlighting the targets and suppressing noise. Finally, the imaging and localization of the pipelines were achieved using the CBP algorithm.

2.1. EM Modeling of Underground Pipelines Using GprMax

GPR is an NDT geophysical technique that utilizes antennas to emit high-frequency pulsed electromagnetic waves (typically 100 MHz–3 GHz) into the subsurface. When the electromagnetic wave comes into contact with boundary or inhomogeneous media, a portion of the energy is reflected. The dielectric permittivity of the medium is determined by combining the time delay and amplitude variations of the signal. GPR offers technical advantages including high-resolution (centimeter-level accuracy), strong real-time performance, and wide environmental adaptability. It is widely used in underground pipeline detection [11], geological structure surveys [12], archaeological site positioning [13], security applications [14], and other nondestructive testing fields [15].

This study employs the gprMax simulator for electromagnetic modeling of underground pipelines. GprMax is an open-source electromagnetic simulation software program specifically designed for GPR numerical simulations. The software solves Maxwell's curl equations using the Finite Difference Time Domain (FDTD) method, enabling an accurate simulation of electromagnetic wave propagation in complex media [16].

The impulse GPR system is one of the most extensively utilized GPR systems in practical applications. When modeling underground pipelines using GprMax, the Ricker wave is commonly used as a source [17]. Mathematically, this zero-phase seismic wavelet is defined as

$$W(t) = -(2\zeta(t-\chi)^2 - 1)e^{-\zeta(t-\chi)^2} \tag{1}$$

In Eq. (1), f is the frequency, $\zeta = \pi^2 f^2$.

Figure 1 shows the time-domain waveform and power spectrum of the Ricker waveform plotted with an amplitude of 1 and a center frequency of 1 GHz. By analyzing Fig. 1, in the time domain, the Ricker wave has characteristics of a symmetrical double-peak structure, a narrow main lobe, and rapidly decaying side lobes, effectively suppressing the interference of multiple reflected waves in the strata, thereby significantly enhancing the vertical resolution of thin-layer targets. In the frequency domain, the energy of the Ricker wave is primarily concentrated around the main frequency, exhibiting a typical single-peak band-pass characteristic, which is beneficial for improving the frequency concentration of the signal. By adjusting the main frequency parameter, a balance can be achieved between the detection depth and resolution according to the electromagnetic propagation characteristics of different media and detection requirements, while effectively reducing the impact of low-frequency noise and high-frequency attenuation on signal integrity.

To achieve the accurate detection of pipeline targets, it is necessary to improve the GPR signal-to-noise ratio (SNR) [18]. In practice, the direct wave exhibits a stronger amplitude than target echoes. Therefore, suppressing the direct-wave interference is critical for pipeline targets. Currently, the background subtraction method is a widely adopted and effective technique [19]. This method involves constructing a background signal model and subtracting it from the radar signal that contains the targets. This method first performs a B-Scan of the underground pipeline to obtain the matrix data of the pipeline, recorded as $S_{pipeline}$. Then, a B-Scan was performed on the background model to obtain the matrix data of the background model, recorded as $S_{background}$. The signal after background subtraction is then expressed as follows.

$$Sr(t) = S_{pipeline} - S_{background} \tag{2}$$

2.2. Adaptive Threshold Scheme for B-Scan Envelope

To enhance the imaging quality, the B-Scan data require further processing. In this study, an adaptive envelope filtering algorithm based on the Hilbert transform was adopted to achieve signal enhancement and background noise suppression [20]. First, the echo data were preprocessed. The negative values in matrix $Sr(t)$ were set to zero [21]. Then, the analytic enve-

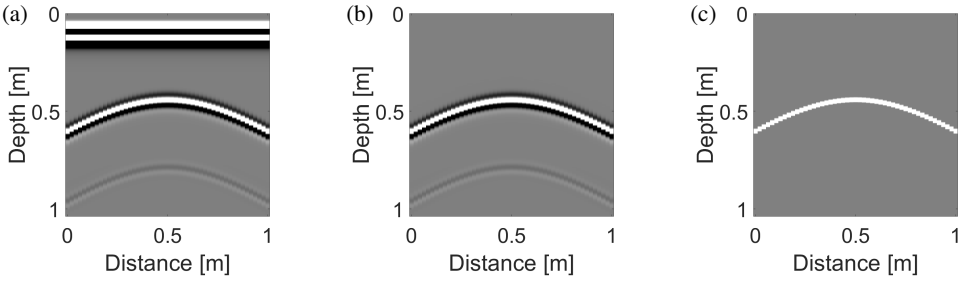

FIGURE 2. B-Scan profiles of underground pipeline. (a) Original B-Scan profile. (b) Background-subtracted B-Scan profile. (c) Envelope of B-Scan profile.

lope of the signal was calculated using the Hilbert transform. The calculation formulas are as follows.

$$Sr(t) = \begin{cases} Sr(t) & \text{if } Sr(t) \geq 0 \\ 0 & \text{if } Sr(t) < 0 \end{cases} \tag{3}$$

$$x(t) = Sr(t) + jH\{Sr(t)\} \tag{4}$$

$$E(t) = |x(t)| = \sqrt{Sr(t)^2 + H\{Sr(t)\}^2} \tag{5}$$

$$T_0 = \alpha \times \max(E(t)) \tag{6}$$

$$T_{k+1} = \max(T_{\min},\ T_k - \Delta t) \tag{7}$$

$$\rho = \frac{\sum_{i=1}^{N}(u_i - \overline{u})(v_i - \overline{v})}{\sqrt{\sum_{i=1}^{N}(u_i - \overline{u})^2}\sqrt{\sum_{i=1}^{N}(v_i - \overline{v})^2}} \tag{8}$$

Eqs. (3)–(5) represent hard thresholding, analytic signal, and envelope, respectively. α and ρ_{target} denote the scale factors of the initial threshold and the target value of envelope signal fidelity, respectively. They are set to 0.28 and 1 in this paper. In Eq. (4), $j = \sqrt{-1}$. In Eq. (7), $\Delta t = 0.01$, $T_{\min} = 0.1$, $T_{\max} = 0.5$. In Eq. (8), u_i, v_i, $\overline{u}$, $\overline{v}$, and N represent the envelope signal, discrete sampled values of the original signal, mean value of the envelope signal, mean value of the original signal, and signal length, respectively. The electromagnetic modeling of underground pipelines was constructed using GprMax 3.0. The simulated models contained metallic (iron) and non-metallic (PVC) pipelines. The electromagnetic parameters of these pipelines are listed in Table 1.

TABLE 1. Electrical parameters in the model.

Material	Relative permittivity (F/m)	Conductivity (S/m)
Copper	1	5.8e7
PVC	3.3	0.00134
Sand	3	0.001

Figures 2(a)–(c) are the original B-Scan profile, the B-Scan profile after background subtraction, and the envelope of the B-Scan, respectively. Comparing Fig. 2(a) and (c), the direct waves and negative amplitude are effectively processed by the background subtraction and adaptive threshold scheme.

2.3. CBP Algorithm for GPR-SAR Imaging

In practical scenarios, the operating environment of GPR is generally not in free space. When both the antenna and targets are situated in a homogeneous medium with relative permittivity, the GPR antenna is typically positioned in air and maintains a distance from the target medium. The scenario depicted in Fig. 3 can be employed for analysis, except that the wave velocity in vacuum c must be substituted by the wave velocity in the medium $v = c/\sqrt{\varepsilon_r}$.

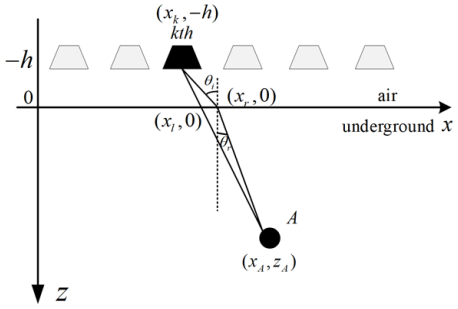

FIGURE 3. The scenario of GPR-SAR imaging.

In Fig. 3, the scenario is divided into two parts by the line $z = 0$. The upper part is air with dielectric constant $\epsilon_1 = \epsilon_0 = 1$ and permeability $\mu_1 = \mu_0 = 1$, where ϵ_0 and μ_0 represent the permittivity and permeability of free space, respectively. The lower part is an isotropic homogeneous medium with relative permittivity $\epsilon_2 = \epsilon_r\epsilon_0$ and permeability $\mu_2 = \mu_0$, where $\epsilon_r > 1$ denotes the relative permittivity of the medium. Owing to the air-medium interface, the electromagnetic wave propagation is refracted at $(x_r, 0)$ rather than following a straight path through $(x_l, 0)$, resulting in two segmented trajectories. The electromagnetic wave is transmitted from the k-th transmitter, passes through the refraction point $(x_r,0)$ to reach point A, and subsequently travels from A through $(x_r, 0)$ to the receiver. According to Snell's law of refraction

$$\frac{\sin\theta_i}{\sin\theta_r} = \sqrt{\varepsilon_r} \tag{9}$$

In Eq. (9), the incident and refraction angles are denoted by θ_i and θ_r, respectively. According to the geometric relationship in Fig. 3, it can be expressed as follows.

$$\frac{(x_r - x_k)^2}{(x_r - x_k)^2 + h^2} \cdot \frac{(x_A - x_r)^2 + z_0^2}{(x_A - x_r)^2} = \varepsilon_r \tag{10}$$

From Eq. (10), determining the refraction point (x_r,0) essentially involves solving the quartic equation in terms of x_r. The two-way travel time can be derived from the solution of x_r

$$\tau_{A,k} = \frac{2\sqrt{(x_r - x_{\bar{k}})^2 + h^2}}{c} + \frac{2\sqrt{(x_A - x_r)^2 + z_A^2}}{v} \quad (11)$$

For N_p antenna positions, the time delays $\{\tau_1, \tau_2, \cdots, \tau_{N_p}\}$ for each target imaging point are first calculated using Eq. (11), then used to extract the back-scattered amplitude of this point from the echo signals.

$$x_k = s_k(t = \tau_k) \quad k = 1, 2, \ldots, N_p \quad (12)$$

In Eq. (12), x_k and s_k(t) represent the amplitude of the scattering response at the k-th antenna position and the echo signal received at the k-th antenna position, respectively, specifically denoting the final envelope signal obtained after the complete preprocessing described in Section 2.2. Through this procedure, an $N_p \times 1$ dimensional vector $\{x_1, x_2, \cdots, x_{Np}\}$ associated with the imaging point is obtained. The BP algorithm neglects the signal correlations between echo channels. The CBP algorithm is used to multiply the N_p elements of vector $\{x_1, x_2, \cdots, x_{Np}\}$ without repetition before stacking. The multiplication strategies are listed in Table 2.

TABLE 2. Cross-correlation multiplication schematic matrix.

	x_1	x_2	$\cdots$	x_{N_p-1}	x_{N_p}
x_1	*	$x_1 \cdot x_2$	$\cdots$	$x_1 \cdot x_{N_p-1}$	$x_1 \cdot x_{N_p}$
x_2	*	*	$\cdots$	$x_2 \cdot x_{N_p-1}$	$x_2 \cdot x_{N_p}$
$\vdots$	*	*	*	$\vdots$	$\vdots$
x_{N_p-1}	*	*	*	*	$x_{N_p-1} \cdot x_{N_p}$
x_{N_p}	*	*	*	*	*

In Table 2, the element at position (i, j) (the i-th row and j-th column of the matrix) represents the product of x_i and x_j, where $i < j$, i.e., only the elements above the matrix diagonal are considered. The remaining combinations are omitted owing to matrix symmetry and are denoted by $*$ in this representation. The superposition process is formulated as follows.

$$E = \sum_{k=1}^{N_p-1} \sum_{l=k+1}^{N_p} x_k \cdot x_l \quad (13)$$

The imaging process is completed by implementing the operation defined in Eq. (13) across all the imaging points.

Standard BP algorithms are based on the 'delay-and-sum' principle, where the pixel intensity is derived from the linear superposition of the echo amplitudes. Although computationally simple, this linear method is prone to artifacts, as strong noise or residual direct waves in a single channel are directly added to the image, creating false targets. In contrast, the CBP algorithm utilized in this study introduces a Spatial Coherence Constraint via a 'delay-multiply-and-sum' strategy. As shown in Table 2, CBP does not perform simple addition but computes the cross-correlation product of signal amplitudes from different antenna pairs. The physical rationale is that valid target echoes from different viewing angles are spatially coherent, yielding large positive values upon multiplication; conversely, random noise and background clutter are typically incoherent across channels, meaning that their products tend to be negligible or cancel out during the summation. Consequently, this multiplication operation acts as a spatial filter, significantly enhancing the target focus and suppressing artifacts compared with traditional BP methods.

3. RESULTS AND ANALYSIS

The diameter of a single pipeline (copper and PVC) is set to 0.1 m with a wall thickness of 0.02 m. The upper surface of the pipeline is buried at 0.4 m underground (defined as the depth of pipeline), and the lateral position is 0.5 m. To validate the focusing capability of the method on non-metallic pipeline geometries, a square pipeline was positioned with its upper surface at 0.3 m depth. The square pipeline has a side length of 0.2 m and its center is located at (0.5 m, 0.4 m). The arched pipeline was buried at 0.3 m depth. The profile consists of an upper semicircular segment with a radius of 0.1 m and a lower square with a side length of 0.2 m.

As shown in Fig. 4(a), the copper pipeline was focused at coordinates (0.5 m, 0.4 m). Owing to the total reflection of electromagnetic waves from the metallic pipelines, only the upper-surface reflection is visible in the imaging results. In Fig. 4(b), the PVC pipeline upper surface was imaged at depth 0.3 m and the center of axis is 0.5 m, with a circular cross-sectional profile. Figs. 4(c)–4(d) show the geometric profiles of square and arched conduits with upper surfaces positioned at 0.3 m depth. The simulation results of PVC pipelines with various geometries confirm that the adaptive threshold enhanced-CBP algorithm enables the detection of underground pipelines, providing positional and geometric parameters critical for pipeline data interpretation.

As shown in Figs. 5(a)–5(b), the multiple pipelines (copper and PVC) are buried at 0.3 m depth and positioned at coordinates (0.5 m, 0.4 m) and (1.5 m, 0.4 m) with a radius of 0.1 m. Two additional simulation models were established to evaluate the resolution performance under dense target scenarios. As shown in Figs. 5(c)–(d), The first model consists of two pipelines centered at (0.9 m, 0.4 m) and (1.1 m, 0.4 m), respectively, resulting in a center-to-center spacing of 0.2 m (i.e., physically touching targets). The second model comprises three pipelines located at (0.6 m, 0.4 m), (0.8 m, 0.4 m), and (1.2 m, 0.4 m). Consequently, the spacing between the first pair is 0.2 m, while the spacing between the second pair is 0.4 m. The Peplinski soil is used in this study to verify the robustness of the method in inhomogeneous soil. In Figs. 6(a) and 6(c), two copper pipelines are positioned in the sand and Peplinskis' soil media. They are buried at 0.3 m and 0.5 m depth and positioned at coordinates (0.5 m, 0.4 m) and (1.5 m, 0.6 m) with a radius of 0.1 m.

As shown in Fig. 5 and Fig. 6, different types of multiple pipelines are focused at coordinates (0.5 m, 0.4 m) and (1.5 m, 0.4 m), and different depths of copper pipelines are focused at coordinate (0.5 m, 0.3 m) and (1.5 m, 0.5 m). The

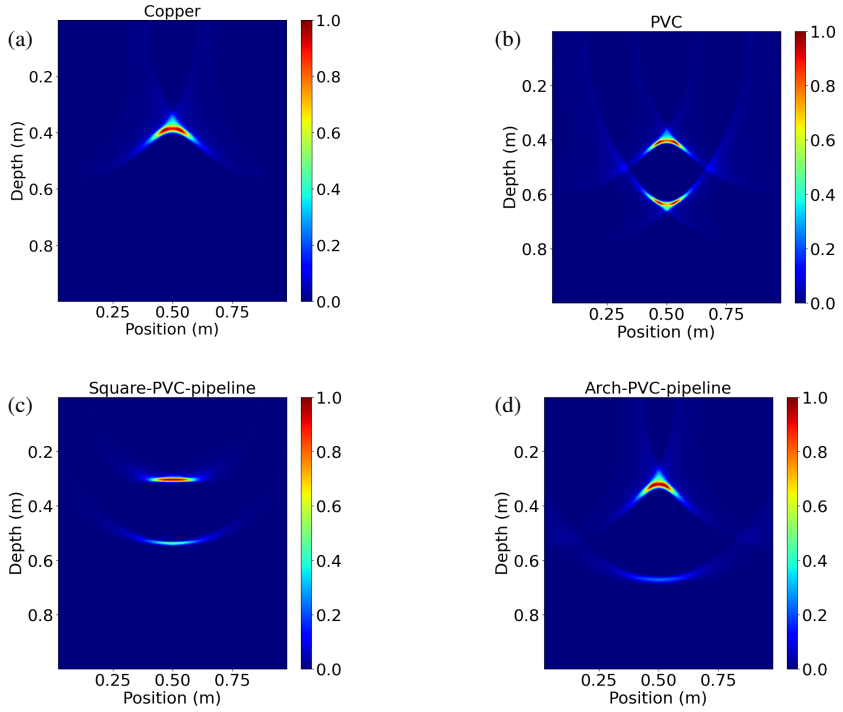

FIGURE 4. The imaging results of the pipeline by CBP. (a) Copper pipeline. (b) PVC pipeline. (c) PVC-square pipeline. (d) PVC-arch pipeline.

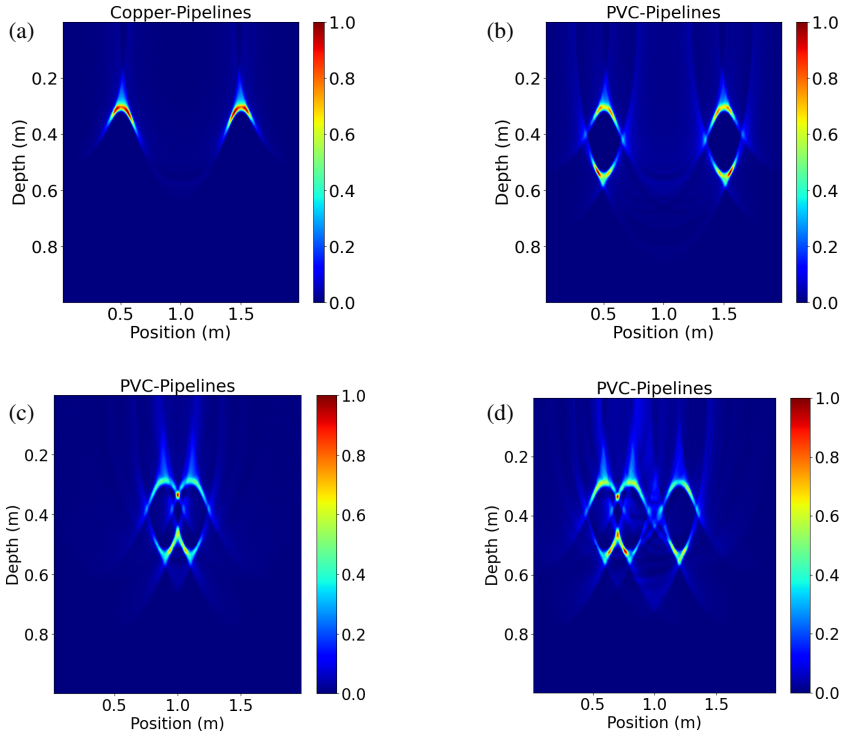

FIGURE 5. The imaging results of multiple pipelines by CBP. (a) Copper pipelines. (b) PVC pipelines. (c) Two adjacent PVC pipelines. (d) Three PVC pipelines positioned at different coordinates.

analysis of Fig. 5 and Fig. 6 demonstrates that both metallic and non-metallic pipelines can achieve precise positional localization and geometric reconstruction when focused imaging is performed using the adaptive threshold enhanced-CBP algorithm. Under multiple pipeline conditions with either close inter-pipeline spacing or significant burial depth variations, the algorithm maintains superior spatial resolution capability to accurately distinguish echo responses and perform imaging of multiple targets. A comparative analysis of Figs. 6(b) and (d) indicates that anisotropic soils exhibit higher electromagnetic wave attenuation than isotropic media. This phenomenon results in reduced echo strength from the second pipeline, as il-

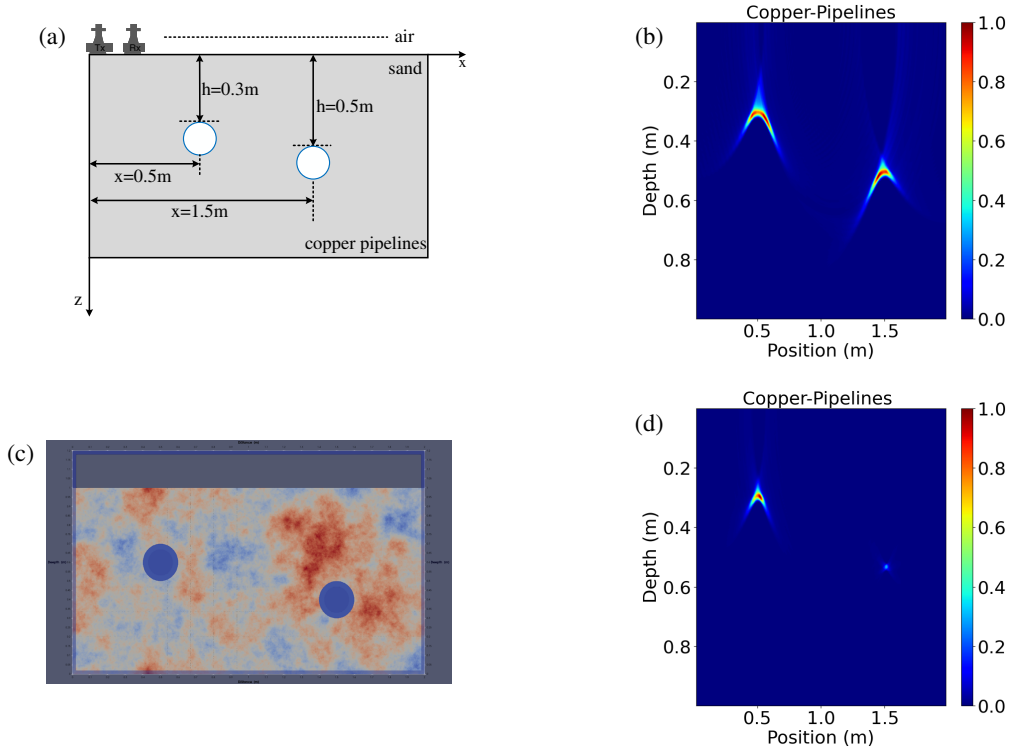

FIGURE 6. The imaging results of copper pipelines with different depths by CBP. (a) The scenario of copper pipelines. (b) Copper pipelines. (c) The scenario of Peplinski's soil. (d) Copper pipelines.

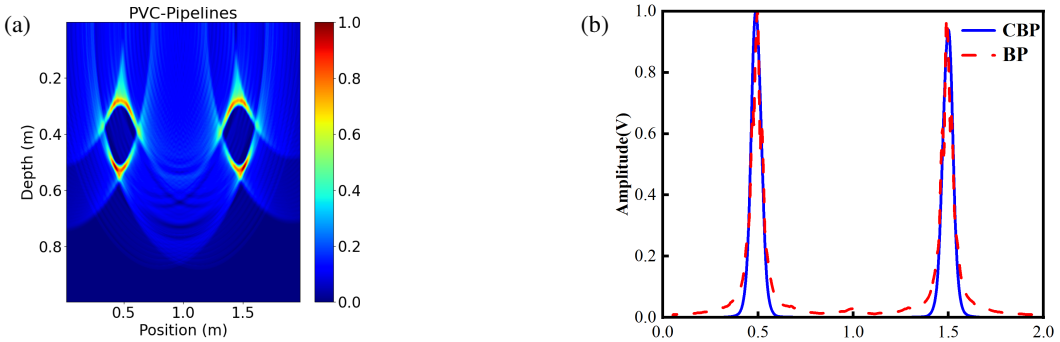

FIGURE 7. The comparison of imaging results between BP and CBP algorithms. (a) The imaging results of the pipeline by BP. (b) The comparison results of maximum amplitude.

lustrated in Fig. 6(d). Nevertheless, even with diminished echo signals, the adaptive threshold enhanced-CBP algorithm effectively determines the spatial positioning and geometric characteristics of pipelines.

To validate the imaging effectiveness of the proposed CBP algorithm, a comparative experiment was conducted by applying the traditional BP algorithm to the identical simulation model shown in Fig. 5(b), and the results are presented in Fig. 7(a). Subsequently, to evaluate the focusing quality quantitatively, the lateral maximum amplitude profiles of both algorithms were extracted and compared (as illustrated in Fig. 7(b)). The analysis of Fig. 7(b) reveals that the CBP algorithm exhibits excellent beam sharpening effects at the target centers. Quantitative data indicate that the Full Width at Half Maximum (FWHM) of the CBP main lobe is approximately 50% of that observed in the BP algorithm. This difference shows that the proposed CBP algorithm outperforms the traditional BP method in terms of both the target focusing performance and imaging resolution.

4. CONCLUSION

This paper presents a CBP algorithm with an adaptive threshold scheme to enhance its capability for GPR-SAR imaging of underground pipelines. Different types and shapes of pipeline models were constructed by using GprMax, validating the adaptability of the method to diverse target geometries. To enhance the target echoes and suppress noise during data preprocessing, the background subtraction method was employed to remove direct wave interference. The adaptive threshold scheme was adopted to obtain the envelopes of B-Scan profiles using the Hilbert transform for enhancing CBP. Three experi-

ments demonstrate that the enhanced-CBP algorithm achieves sub-wavelength localization for different types of pipelines and reconstruction ability for non-metallic pipelines. The proposed method demonstrates enhanced accuracy in the positioning of metal pipelines and effectively reconstructs the geometries of non-metallic pipelines with weak reflections, exhibiting robustness in complex soil conditions and diverse target environments in GPR-SAR imaging. This study establishes a technical foundation for high-precision GPR-SAR imaging, providing critical infrastructure information for urban pipeline safety assessment and aging network maintenance. However, it should be noted that the absence of measured field data represents a limitation of the current study, as a controlled simulation environment was prioritized to validate the core principles with precise Ground Truth. Therefore, future work should focus on conducting physical model experiments and field measurements.

ACKNOWLEDGEMENT

This work was supported in part by the National Natural Science Foundation of China (NSFC) under Grant 62461054, Grant 62501519, and Grant 62361054, and in part by the Natural Science Basic Research Plan in Shaanxi Province of China under Grant No. 2025JC-YBMS-684.

REFERENCES

[1] Demirci, S., E. Yigit, I. H. Eskidemir, and C. Ozdemir, "Ground penetrating radar imaging of water leaks from buried pipes based on back-projection method," *NDT & E International*, Vol. 47, 35–42, 2012.

[2] Ren, K. and R. J. Burkholder, "A uniform diffraction tomographic imaging algorithm for near-field microwave scanning through stratified media," *IEEE Transactions on Antennas and Propagation*, Vol. 64, No. 12, 5198–5207, 2016.

[3] Phillips, L. C., L. A. Eichel, and S. M. Evanko, "Ultrawideband SAR processing with the range migration algorithm and the imsyn processor," in *SPIE's 1996 International Symposium on Optical Science, Engineering, and Instrumentation*, Vol. 2845, 205–210, 1996.

[4] Mast, J. E. and E. M. Johansson, "Three-dimensional ground-penetrating radar imaging using multifrequency diffraction tomography," in *SPIE's 1994 International Symposium on Optics, Imaging, and Instrumentation*, Vol. 2275, 196–203, 1994.

[5] Schmelzbach, C., J. Tronicke, and P. Dietrich, "Three-dimensional hydrostratigraphic models from ground-penetrating radar and direct-push data," *Journal of Hydrology*, Vol. 398, No. 3-4, 235–245, 2011.

[6] Leuschen, C. J. and R. G. Plumb, "A matched-filter-based reverse-time migration algorithm for ground-penetrating radar data," *IEEE Transactions on Geoscience and Remote Sensing*, Vol. 39, No. 5, 929–936, 2001.

[7] Catapano, I., A. Randazzo, E. Slob, and R. Solimene, "GPR imaging via qualitative and quantitative approaches," in *Civil Engineering Applications of Ground Penetrating Radar*, 239–280, Springer, 2015.

[8] Foo, S. and S. Kashyap, "Cross-correlated back projection for UWB radar imaging," in *IEEE Antennas and Propagation Society Symposium, 2004.*, Vol. 2, 1275–1278, Monterey, CA, USA, 2004.

[9] Lim, H. B., N. T. T. Nhung, E.-P. Li, and N. D. Thang, "Confocal microwave imaging for breast cancer detection: Delay-multiply-and-sum image reconstruction algorithm," *IEEE Transactions on Biomedical Engineering*, Vol. 55, No. 6, 1697–1704, 2008.

[10] Zhou, L., C. Huang, and Y. Su, "A fast back-projection algorithm based on cross correlation for GPR imaging," *IEEE Geoscience and Remote Sensing Letters*, Vol. 9, No. 2, 228–232, 2012.

[11] Guo, Q., P. Yang, R. Wu, and Y. Zhang, "Numerical modeling of GPR for underground multi-pipes detection by combining gprmax and deep learning model," *Progress In Electromagnetics Research M*, Vol. 128, 99–113, 2024.

[12] Rezaei, A., H. Hassani, P. Moarefvand, and A. Golmohammadi, "Determination of unstable tectonic zones in C-North deposit, Sangan, NE Iran using GPR method: Importance of structural geology," *Journal of Mining and Environment*, Vol. 10, No. 1, 177–195, 2019.

[13] Linck, R., M. Kale, A. Stele, and J. Schlechtriem, "Testing the applicability of drone-based ground-penetrating radar for archaeological prospection," *Remote Sensing*, Vol. 17, No. 9, 1498, 2025.

[14] Jamshidi-Zarmehri, H., A. Akbari, M. Labadlia, K. E. Kedze, J. Shaker, G. Xiao, and R. E. Amaya, "A review on through-wall communications: Wall characterization, applications, technologies, and prospects," *IEEE Access*, Vol. 11, 127 837–127 854, 2023.

[15] Hoxha, E., J. Feng, D. Sanakov, and J. Xiao, "Robotic inspection and subsurface defect mapping using impact-echo and ground penetrating radar," *IEEE Robotics and Automation Letters*, Vol. 8, No. 8, 4943–4950, 2023.

[16] Warren, C., A. Giannopoulos, and I. Giannakis, "GprMax: Open source software to simulate electromagnetic wave propagation for Ground Penetrating Radar," *Computer Physics Communications*, Vol. 209, 163–170, 2016.

[17] Ramadhan, A. R., E. Ali, and A. A. Pramudita, "The effect ricker wavelet of duty cycle adjustment on GPR detection result," *JMECS (Journal of Measurements, Electronics, Communications, and Systems)*, Vol. 8, No. 1, 17–22, 2021.

[18] Li, J., C. L. Bastard, Y. Wang, G. Wei, B. Ma, and M. Sun, "Enhanced GPR signal for layered media time-delay estimation in low-SNR scenario," *IEEE Geoscience and Remote Sensing Letters*, Vol. 13, No. 3, 299–303, 2016.

[19] Sharma, P., B. Kumar, D. Singh, and S. P. Gaba, "Critical analysis of background subtraction techniques on real GPR data," *Defence Science Journal*, Vol. 67, No. 5, 559–571, 2017.

[20] Sharma, P., B. Kumar, and D. Singh, "Development of adaptive threshold and data smoothening algorithm for GPR imaging," *Defence Science Journal*, Vol. 68, No. 3, 316–325, 2018.

[21] Venkatachalam, A. S., X. Xu, D. Huston, and T. Xia, "Development of a new high speed dual-channel impulse ground penetrating radar," *IEEE Journal of Selected Topics in Applied Earth Observations and Remote Sensing*, Vol. 7, No. 3, 753–760, 2014.